

**Allanite at high pressure: effect of REE on the elastic  
behaviour of epidote-group minerals**

**G. Diego Gatta, Sula Milani, Luca Corti, Davide Comboni, Paolo Lotti,  
Marco Merlini, Hanns-Peter Liermann**

**Running title:** *HP* behavior of allanite

**Abstract**

**Introduction**

**Materials and experimental methods**

**Results: Elastic behaviour of allanite at high-pressure**

**Results: Deformation mechanisms at the atomic scale**

**Discussion and conclusions**

**Acknowledgements**

**References**

**Figures/Tables**

**Corresponding author: G. Diego GATTA**

Dipartimento Scienze della Terra  
Università degli Studi di Milano  
Via Botticelli, 23  
I-20133 Milano, Italy  
Tel. +39 02 503 15607  
Fax +39 02 503 15597  
E-Mail: diego.gatta@unimi.it

# Allanite at high pressure: effect of REE on the elastic behaviour of epidote-group minerals

<sup>1</sup>G. Diego Gatta, <sup>1</sup>Sula Milani, <sup>1</sup>Luca Corti, <sup>1</sup>Davide Comboni, <sup>1</sup>Paolo Lotti, <sup>1</sup>Marco Merlini, <sup>2</sup>Hanns-Peter Liermann

<sup>1</sup>Dipartimento di Scienze della Terra, Università degli Studi di Milano,  
Via Botticelli 23, I-20133 Milano Italy

<sup>2</sup>Photon Sciences, DESY, PETRA-III, Notkestrasse 85, D-22607, Hamburg, Germany

## Abstract

The compressional behaviour of a natural allanite from Lago della Vecchia (upper Cervo valley, Italy) metagranitoids

$[^{A1}(\text{Ca}_{0.69}\text{Fe}^{2+}_{0.31})_{\Sigma 1.00}{}^{A2}(\text{Ca}_{0.46}\text{Ce}_{0.24}\text{La}_{0.12}\text{Sm}_{0.02}\text{Pr}_{0.05}\text{Nd}_{0.09}\text{Th}_{0.02})_{\Sigma 1.00}$

$^{M1}(\text{Al}_{0.65}\text{Fe}^{3+}_{0.34}\text{Ti}_{0.02})_{\Sigma 1.01}{}^{M2}(\text{Al}_{0.99}){}^{M3}(\text{Fe}^{3+}_{0.54}\text{Fe}^{2+}_{0.36}\text{Mg}_{0.06}\text{Ti}^{4+}_{0.02}\text{Al}_{0.01})_{\Sigma 0.99}$

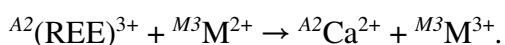
$^{Si1, Si2, Si3}(\text{Si}_{2.80}\text{Al}_{0.20})_{\Sigma 3.00}\text{O}_{11}(\text{OH}, \text{O})]$  has been investigated up to 16 GPa (at 298 K) by means of *in-situ* synchrotron single-crystal X-ray diffraction. Experiments have been conducted under hydrostatic conditions, using a diamond anvil cell and the mix methanol:ethanol:water=16:3:1 (up to 10 GPa) and neon (up to 16 GPa) as pressure-transmitting media. No phase transition has been observed within the pressure-range investigated; data collected in decompression prove that, at least up to 16 GPa (at 298 K), the deformation mechanisms are fully reversible. A third-order Birch-Murnaghan Equation of State (BM-EoS) was fitted to the *P-V* data (up to 10 GPa), giving:  $V_0 = 470.2(2) \text{ \AA}^3$ ,  $K_{P_0, T_0} = 131(4) \text{ GPa}$  and  $K' = 1.9(8)$ . The evolution of the lattice parameters with pressure shows a slight anisotropic compression pattern, with  $K_{P_0, T_0}(a):K_{P_0, T_0}(b):K_{P_0, T_0}(c) = 1.24:1.52:1$ . The monoclinic  $\beta$ -angle decreases monotonically with pressure, with:  $\beta_P(^{\circ}) = \beta_{P_0} - 0.0902(4)P$  ( $R^2 = 0.997$ , with  $P$  in GPa).

The main deformation mechanisms at the atomic scale are described based on a series of structure refinements at different pressures. A comparison between the compressional behavior of allanite, epidote and clinozoisite is carried out.

**Keywords:** allanite, epidote, synchrotron single-crystal X-ray diffraction, high-pressure, compressibility.

## 70 Introduction

71 Allanite is a sorosilicate and a member of the epidote group, with general  
72 crystal formula  $A(1)A(2)M(1)M(2)M(3)(\text{SiO}_4)(\text{Si}_2\text{O}_7)\text{O}(\text{OH})$ , where the  $A(1)$  and  $A(2)$   
73 are sites with coordination number  $\text{CN}>6$  and mainly occupied by Ca, and  $M(1)$ ,  $M(2)$   
74 and  $M(3)$  are octahedral sites ( $\text{CN}=6$ ) mainly occupied by Al and  $\text{Fe}^{3+}$  (Dollase 1971;  
75 Franz and Liebscher 2004; Armbruster et al. 2006). All the members of the epidote  
76 group are monoclinic in symmetry, with structure topology consistent with the space  
77 group  $P2_1/m$ , although possible symmetry reduction in some epidotes (to  $Pm$ ,  $P2_1$  or  
78  $P\bar{1}$ ) has been suggested as effect of cation ordering (Franz and Liebscher 2004). The  
79 structure of the epidote group minerals has single silicate tetrahedra ( $\text{SiO}_4$ ), double  
80 silicate tetrahedra ( $\text{Si}_2\text{O}_7$ ), and continuous chains of  $\text{MO}_6$  and  $\text{MO}_4(\text{OH})_2$  octahedra  
81 (parallel to the  $b$ -axis) as main building-block units. The octahedra are bridged by  
82 single  $\text{SiO}_4$  and double  $\text{Si}_2\text{O}_7$  tetrahedral groups, in a configuration as that shown in  
83 (Fig. 1). Clinozoisite (ideally  $^{A1,A2}\text{Ca}_2^{M1,M2,M3}\text{Al}_3(\text{SiO}_4)(\text{Si}_2\text{O}_7)\text{O}(\text{OH})$ ) can be  
84 considered as the reference structure of the epidote group minerals, in which the three  
85 independent octahedral  $M$  sites ( $M1$ ,  $M2$  and  $M3$ ) are fully occupied by Al and the  
86 two independent  $A$  sites ( $A1$  and  $A2$ ) are occupied by Ca. The complex crystal-  
87 chemistry of the epidote group led the Commission of the International Mineralogical  
88 Association to divide it into three subgroups (Armbruster et al. 2006). The allanite  
89 subgroup contains rare-earth elements (REE) rich minerals, typified by the  
90 eponymous mineral “allanite”. The crystal chemistry of the allanite subgroup  
91 members may be derived from that of clinozoisite, by homovalent substitutions and  
92 one coupled heterovalent substitution, as follows:



94 In this light, the (cationic) site population is represented by:  $A1 = \text{M}^{2+}$ ,  $A2 = \text{M}^{3+}$ ,  $M1$   
95  $= \text{M}^{3+}$ ,  $M2 = \text{M}^{3+}$ , and  $M3 = \text{M}^{2+}$ , and the general formula of allanite is:

96  $^{A1}(\text{Ca})^{A2}(\text{REE}^{3+})^{M1,M2}(\text{Al})_2^{M3}(\text{Fe}^{2+})(\text{SiO}_4)(\text{Si}_2\text{O}_7)\text{O}(\text{OH})$  (Dollase 1971; Gieré and  
97 Sorensen 2004; Armbruster et al. 2006).

98 Epidotes mainly occur in low-grade metamorphic rocks (250–400°C, 1-2  
99 kbars). However, Poli and Schmidt (1998) showed that epidotes are stable over a wide  
100 range of pressure and temperature in continental and oceanic crust. Magmatic  
101 epidotes were also reported and described by Schmidt and Poli (2004). A series of  
102 studies showed how the stability of epidote group minerals is not only influenced by

103 pressure and temperature, but also by the Al/Fe<sup>3+</sup> ratio, oxygen fugacity, fluid  
104 composition and solution pH (*e.g.*, Holdaway 1972; Liou 1973; Bird and Helgeson  
105 1980; Bird et al. 1988; Klemd 2004). In addition, a series of *in-situ* high-pressure  
106 (HP) and high-temperature (HT) experiments have been devoted to epidote group  
107 minerals, and in particular to clinozoisite and epidote *sensu stricto*, in order to derive  
108 volume and axial compressibility or thermal expansion (*e.g.*, Catti et al. 1988;  
109 Holland et al. 1996; Pawley et al. 1996; Comodi and Zanazzi 1997; Franz and  
110 Liebscher 2004; Liebscher 2004; Gatta et al. 2010, 2011a, 2011b; Qin et al. 2016),  
111 along with *P*- or *T*-induced deformation mechanisms at the atomic scale (*e.g.*, Comodi  
112 and Zanazzi 1997; Gatta et al. 2010, 2011a). However, to the best of our knowledge,  
113 no experiments have so far been devoted to the behaviour of allanite at non-ambient  
114 conditions by *in-situ* experiments. Consequently, bulk and axial compressibilities or  
115 thermal expansion coefficients of this mineral are completely unknown, and the role  
116 played by the REE replacing Ca at the *A* sites, or the occurrence of Fe<sup>2+</sup> at the  
117 octahedral *M* sites, is still obscure. In this light, the aim of this study is the  
118 investigation of the HP-behavior of a natural allanite, from Lago della Vecchia (upper  
119 Cervo valley, Italy), by *in-situ* synchrotron single-crystal diffraction with a diamond  
120 anvil cell, in order to: provide reliable thermodynamic parameters for petrologic  
121 modeling, report any potential *P*-induced phase transition and describe the main  
122 deformation mechanisms at the atomic scale *via* single-crystal structure refinements.  
123 A comparison between the compressional parameters of allanite and those of epidote  
124 *sensu stricto* and clinozoisite is carried out.

125

126

127

## 128 **Materials and experimental methods**

129 Natural single-crystals of allanite from Lago della Vecchia (upper Cervo valley, Italy)  
130 metagranitoids were used in this study. The host rock is characterized by  
131 heterogenous deformation due to stain partitioning (Corti et al. 2017) during  
132 development of *HP-LT* blueschist-facies dominant fabric, which represent a re-  
133 equilibration following the metamorphic peak in the eclogite facies, under thermally  
134 depressed conditions (Corti et al. 2018). Chemical microanalyses in wavelength-  
135 dispersive mode (EPMA-WDS) were performed on a series of optically homogeneous  
136 sub-millimetric crystals, using a JEOL JXA-8200 microprobe at the Earth Sciences  
137 Department, University of Milano. The system was operated using an accelerating  
138 voltage of 15 kV, a beam current of 5 nA, a beam diameter of 5  $\mu\text{m}$ , and a counting  
139 time of 30 s on the peaks and 10 s on the backgrounds. A series of natural and  
140 synthetic standards were used. The raw data were corrected for matrix effects using  
141 the protocol implemented in the JEOL suite of programs. The crystals of allanite,  
142 selected for this study, were found to be compositionally homogeneous. The average  
143 unit-formula, based on more than 40 point-analyses and calculated following the  
144 protocol recommended by IMA Commission (Armbruster et al. 2006), on the basis of  
145 13 oxygen atoms, is:  
146  $A^1(\text{Ca}_{0.69}\text{Fe}^{2+}_{0.31})_{\Sigma 1.00}A^2(\text{Ca}_{0.46}\text{Ce}_{0.24}\text{La}_{0.12}\text{Sm}_{0.02}\text{Pr}_{0.05}\text{Nd}_{0.09}\text{Th}_{0.02})_{\Sigma 1.00}$   
147  $M^1(\text{Al}_{0.65}\text{Fe}^{3+}_{0.34}\text{Ti}_{0.02})_{\Sigma 1.01}M^2(\text{Al}_{0.99})M^3(\text{Fe}^{3+}_{0.54}\text{Fe}^{2+}_{0.36}\text{Mg}_{0.06}\text{Ti}^{4+}_{0.02}\text{Al}_{0.01})_{\Sigma 0.99}$   
148  $^{Si1, Si2, Si3}(\text{Si}_{2.80}\text{Al}_{0.20})_{\Sigma 3.00}\text{O}_{11}(\text{OH}, \text{O})$ . Further details pertaining to experimental  
149 protocols and EPMA-WDS data statistics are given in Corti et al. (2019).

150 High-pressure synchrotron X-ray single-crystal diffraction experiments were  
151 performed at the Extreme Conditions Beamline P02.2 at DESY/PETRA-III. X-rays  
152 with an energy of 42.7 keV (0.2904  $\text{\AA}$  wavelength) were used, with a focusing spot of  
153  $\sim 8.5$  (H) x 1.8 (V)  $\mu\text{m}^2$  originating from a compound refractive lenses (CRL) system  
154 consisting of 110 Be lenses with a radius of 50  $\mu\text{m}$  (400  $\mu\text{m}$  beam acceptance) and a  
155 focal length of 1,221 mm. Two prismatic single-crystals of allanite ( $\sim 50$  x 50 x 15  
156  $\mu\text{m}^3$ ) were selected for the *HP* experiments, loaded, respectively, in two symmetric  
157 diamond anvil cells (DAC), equipped with Bohler–Almax design diamonds/seats  
158 with a 70° opening and 300- $\mu\text{m}$  culets size. For the first DAC, a 250- $\mu\text{m}$ -thick  
159 rhenium gasket was pre-indented to 50  $\mu\text{m}$  and then drilled with 150  $\mu\text{m}$  hole, in  
160 which the crystal of allanite along with some calibrated ruby spheres (for pressure

161 determination, according to Mao et al. 1986) were placed. Neon was used as  
162 hydrostatic pressure transmitting medium (Klotz et al. 2009). For the second DAC, a  
163 250- $\mu\text{m}$ -thick steel gasket was pre-indented to 60  $\mu\text{m}$  and then drilled with 150  $\mu\text{m}$   
164 hole, in which the crystal of allanite and ruby micro-spheres were located. In this case,  
165 the methanol:ethanol:water = 16:3:1 mix was used as hydrostatic  $P$ -transmitting fluid  
166 up to 10 GPa (Angel et al. 2007). For both the experiments, pressure was increased  
167 with an automated pressure-driven system and measured with the online  
168 ruby/alignment system. Diffraction images were acquired on a PerkinElmer XRD  
169 1621 flat panel detector, using an in-house script for collecting step-scan diffraction  
170 images. Sample to detector distance (402.34 mm) was calibrated using a  $\text{CeO}_2$   
171 standard (NIST 674a). The diffraction images were then converted to conform to the  
172 “Esperanto” format of the program CrysAlis (Rigaku – Oxford Diffraction 2018;  
173 Rothkirch et al. 2013). The diffraction data were first collected with the crystals in the  
174 DAC and without any  $P$ -medium (*i.e.* ambient pressure). A pure  $\omega$ -scan ( $-33^\circ \leq \omega \leq$   
175  $+33^\circ$ ), with a step size of  $0.5^\circ$  and an exposure time of 0.5 s/frame, was used during  
176 data collection. X-ray diffraction peaks were then indexed and their intensities were  
177 integrated and corrected for Lorentz-polarization (Lp) effects, using the CrysAlis  
178 package. Scaling and correction for absorption (due to the DAC components) was  
179 applied by the semi-empirical *ABSPACK* routine implemented in CrysAlis. The  
180 reflection conditions were consistent with those of the space group  $P2_1/m$ . *HP* data for  
181 the experiments with methanol:ethanol:water mix as  $P$ -fluid were collected up to  $\sim 8.5$   
182 GPa; those pertaining to the experiment with neon as  $P$ -transmitting medium up to  
183  $\sim 16.3$  GPa (the hydrostatic limit of neon, according to Klotz et al. 2009). No evidence  
184 of phase transitions was observed within the  $P$ -range investigated. Data collected in  
185 decompression proved that allanite behaves elastically at least up to 16 GPa (at 298  
186 K) (Table 1) under hydrostatic conditions. The unit-cell parameters of allanite with  $P$ ,  
187 based on the two different ramps (*i.e.*, in methanol:ethanol:water mix and in neon) are  
188 listed in Table 1.

189 The isotropic structure refinements, based on the intensity data of the two *HP*  
190 ramps, were conducted using the software SHELXL97 (Sheldrick 1997, 2008),  
191 starting from the structure model of Dollase (1971) and Bonazzi et al. (2009), in the  
192 space group  $P2_1/m$ . To reduce the number of variables to refine, and considering the  
193 average chemical composition of the allanite of this study, the atomic sites were

194 modelled as follows: the *A1* and *A2* sites were modelled with a mixed (Ca + Ce) X-  
 195 ray scattering curve, and the fraction of Ca vs. Ce were refined; the *M1* and *M2*  
 196 octahedral sites as populated by Al only and the *M3* site as populated by (Fe + Al),  
 197 and the fraction Fe vs. Al were refined; the three independent tetrahedral sites (*i.e.*,  
 198 *Si1*, *Si2* and *Si3*) were modelled as fully occupied by Si. For all the refinements,  
 199 convergence was rapidly achieved and, at the end of the last cycles of refinement, no  
 200 significant correlation was observed in the variance-covariance matrix of the refined  
 201 parameters. The principal statistical parameters of the structure refinements are listed  
 202 in Table 2. Atomic coordinates and site occupancies of selected structure refinements  
 203 are given in Table S1. Bond distances and other relevant structural parameters are  
 204 reported in Tables S2 and 3.

205

### 206 **Results: Elastic behaviour of allanite at high-pressure**

207 The evolution of the lattice parameters of allanite with pressure is shown in  
 208 Fig. 2 and Fig. S1, which shows that no phase transition or change of the deformation  
 209 mechanisms occur within the *P*-range investigated (*i.e.*, at least up to 16 GPa at 298  
 210 K). A second- and a third-order Birch-Murnaghan Equation of State (BM-EoS) (Birch  
 211 1947; Angel 2000) were fitted to the *P-V* data pertaining to the experiment with  
 212 methanol:ethanol:water mix as *P*-transmitting fluid (*i.e.*, the most populated *P*-ramp),  
 213 using the EOS-FIT program (by RJ Angel, www.rossangel.com). This isothermal EoS  
 214 is based on the assumption that the high-pressure strain energy in a solid can be  
 215 expressed as a Taylor series in the Eulerian finite strain, defined as  $fe = [(V_0/V)^{2/3} -$   
 216  $1]/2$ , and allows to obtain the bulk modulus ( $K_{P_0,T_0} = V(\partial P/\partial V)_{T_0} = \beta^{-1}_{P_0,T_0}$ , where  
 217  $\beta_{P_0,T_0}$  is the volume compressibility coefficient at room conditions) and its *P*-  
 218 derivatives. Expansion in the Eulerian strain polynomial has the following form:

$$219 \quad P(fe) = 3K_{P_0,T_0} fe (1 + 2fe)^{5/2} \{ 1 + 3/2(K' - 4)fe + 3/2[K_{P_0,T_0}K'' + (K' - 4)(K' - 3) + 35/9]$$

$$220 \quad fe^2 + \dots \}, \text{ where } K' = \partial K_{P_0,T_0} / \partial P \text{ and } K'' = \partial^2 K_{P_0,T_0} / \partial P^2.$$

221 The BM-EoS parameters, simultaneously refined using the data weighted by their  
 222 uncertainties in *P* and *V*, are listed in Table 4. Using a second-order BM-EoS fit,  
 223 convergence is achieved with:  $V_0 = 470.6(2)\text{\AA}^3$  and  $K_{P_0,T_0} = 122(1)$  GPa. A better fit is  
 224 obtained using a third-order BM-EoS with:  $V_0 = 470.2(2)\text{\AA}^3$ ,  $K_{P_0,T_0} = 131(4)$  GPa and  
 225  $K' = 1.9(8)$ . The use of a third-order BM-EoS in energy, to model the compressional  
 226 behaviour of allanite, is also corroborated by the evolution of the Eulerian finite strain

227 vs. “normalized stress” plot ( $fe-Fe$  plot, with  $Fe = P/[3fe(1+2fe)^{5/2}]$ ; Angel 2000),  
228 shown in Fig. 3: the weighted linear regression through the data points yields  $Fe(0)=$   
229 131(2) GPa as intercept values and the (negative) slope of the regression line gives  
230 rise to a  $K'$  value of 1.9(6), in good agreement with the third-order BM-EoS fit.

231 The confidence ellipses at 68.3% level ( $\Delta\chi^2 = 2.30, \pm 1\sigma$ ), 95.4% level ( $\Delta\chi^2$   
232  $= 6.17, \pm 2\sigma$ ) and 99.7% level ( $\Delta\chi^2 = 11.8, \pm 3\sigma$ ) were calculated starting from the  
233 variance-covariance matrix of  $K_{P0,T0}$  and  $K'$  obtained from the least-square procedure  
234 (third-order BM-EoS fit previously described; Angel 2000). The ellipses are strongly  
235 elongated with negative slope (Fig. 4), showing a negative correlation of the  
236 parameters  $K_{P0,T0}$  and  $K'$ .

237 The evolution of the lattice parameters with pressure shows a slight anisotropic  
238 compressional pattern. The “axial bulk moduli”, calculated with a second-order  
239 “linearized” BM-EoS (Angel 2000 for details), are:  $K_{P0,T0}(a) = 114(2)$  GPa for the  $a$ -  
240 axis,  $K_{P0,T0}(b) = 140(4)$  GPa for the  $b$ -axis, and  $K_{P0,T0}(c) = 92(1)$  GPa for the  $c$ -axis,  
241 with a general anisotropic compressional scheme:  
242  $K_{P0,T0}(a):K_{P0,T0}(b):K_{P0,T0}(c) = 1.24:1.52:1$  (Table 4). The second-order BM-EoS fits  
243 provide the best figure of merit. The monoclinic  $\beta$ -angle decreases linearly with  
244 pressure, with:  $\beta_P(^{\circ}) = \beta_{P0} (^{\circ}) - 0.0902(4)P$  ( $R^2 = 0.997$ , with  $P$  in GPa) (Fig. 2 and  
245 S1).

246 Magnitude and orientation of the principal unit-strain coefficients between  
247 room pressure and the maximum  $P$  achieved (*i.e.*,  $\Delta P = 8.51$  GPa, ramp in  
248 methanol:ethanol:water mix), derived on the basis of the finite Eulerian strain tensor,  
249 were calculated with the *Win\_Strain* software (by RJ Angel, www.rossangel.com).  
250 The following Cartesian axial system was chosen:  $x//a^*$  and  $y//b$ . The strain ellipsoid  
251 is oriented with the mid axis ( $\epsilon_2$ ) parallel to the  $b$ -axis, and the major ( $\epsilon_1$ ) and minor  
252 ( $\epsilon_3$ ) axes lying in the (010)-plane:  $\epsilon_1$  describes an angle of  $136.6(2)^{\circ}$  from  $a$  (and thus  
253  $22.3(2)^{\circ}$  from  $c$ ), as shown in Fig. 1. The elastic behaviour of allanite based on the  
254 unit-strain coefficients between 0.0001 and 8.51 GPa is more anisotropic if compared  
255 to that deduced only along the principal crystallographic directions, being  $\epsilon_1 = -$   
256  $0.02849(5)$ ,  $\epsilon_2 = -0.0192(5)$ , and  $\epsilon_3 = -0.01306(8)$  GPa $^{-1}$ , with the resulting anisotropic  
257 scheme:  $\epsilon_1:\epsilon_2:\epsilon_3 = 2.18:1.47:1$ .

258 As only a few data-points were collected in Ne (Tables 1 and 2), such an  
259 experiment was mainly aimed to demonstrate that, at least up to 16 GPa, allanite is  
260 still crystalline. Thus, Ne-data were not used for the compressional analysis.

261

## 262 **Results: Deformation mechanisms at the atomic scale**

263 The mechanisms at the atomic scale that govern the anisotropic compression of  
264 the allanite structure can be described in terms of intra- and inter-polyhedral re-  
265 arrangement in response to the applied pressure. Intra-polyhedral deformations are  
266 usually described in terms of compression of the bond distances or by distortion (*i.e.*,  
267 with or without bond-distances compression), inter-polyhedral rearrangements in  
268 terms of polyhedral tilting.

269 If we consider the *P*-induced atomic displacements in allanite structure, the  
270 oxygen sites *O8* and *O9* show the most pronounced displacements from their  
271 positions refined at 0.0001 GPa. *O9* is the bridging oxygen between the *T1* and *T2*  
272 tetrahedra, describing the angle *T1-O9-T2* of  $\sim 145.5^\circ$  at 0.0001 GPa, which decreases  
273 to  $\sim 140.4^\circ$  at 8.5 GPa (Table S2); the difference is remarkable, if we consider the *P*-  
274 range. This tilting mechanism, governed by the displacement of the *O9* site, affects  
275 the shape of the 5-membered rings of polyhedra (*M2-T3-M2-T2-T1*, Fig. 1), confining  
276 the cavities in which the *A1* site lies: the contraction of the  $O3 \leftrightarrow O1$ ,  $O6 \leftrightarrow O1$  and  
277  $O9 \leftrightarrow O5$  “diameters” is significantly different, being respectively  $\sim 0.09$ ,  $\sim 0.06$ , and  
278  $\sim 0.03$  Å within the *P*-range 0.0001-8.5 GPa. *O9* is also bonded to the *A1* site, and the  
279 displacement of the *O9* leads to a change of the *A1-O9* bond length:  $\sim 3.095$  Å at  
280 0.0001 GPa and  $\sim 3.074$  Å at 8.5 GPa (Table S2).

281 *O8* is the bridging oxygen between the *T2* and *M3* polyhedra. The *T2-O8-M3*  
282 angle is  $\sim 130.3^\circ$  at 0.0001 GPa and drastically decreases to  $\sim 123.0^\circ$  at 8.5 GPa (Table  
283 S2). The displacement of the *O8* site, and the aforementioned and co-related  
284 polyhedral tilting, affect the shape evolution with *P* of the 8-membered rings of  
285 polyhedra (*M2-T3-M3-T2-M2-T3-M3-T2*), in which the *A2* site lies (Fig. 1). More  
286 specifically, the  $O8 \leftrightarrow O8$  “diameter” is pronouncedly shortened by  $\sim 0.30$  Å at 8.51  
287 GPa and, in the same *P*-range, the  $O3 \leftrightarrow O3$ ,  $O6 \leftrightarrow O10$  and  $O6 \leftrightarrow O6$  diameters are  
288 shortened by  $\sim 0.20$  Å,  $\sim 0.15$  Å, and  $\sim 0.16$  Å, respectively (Fig. 1, Table 3). This leads  
289 to a more rectangular-edged ring at high pressure, affecting mainly the length of the  
290 unit-cell edge parallel to the *c*-axis.

291 The aforementioned polyhedral tilting mechanisms are coupled with the intra-  
292 polyhedral distortion and compression in response to the applied pressure, which are  
293 energetically more costly and, therefore, less pronounced at low- or mid- $P$  regimes.  
294 The evolution of the intra-polyhedral bond distances and angles shows that, within the  
295  $P$ -range investigated, tetrahedra behaves as quasi-rigid units at a first approximation  
296 (with minor bond-distances shortening or polyhedral distortion), octahedra are more  
297 affected by compression and distortion (though not dramatic), whereas the large  $A1$ -  
298 and  $A2$ -polyhedra are the most affected by distortion and bond-distances shortening in  
299 response to the applied pressure (Table S2). However, the quality of the structural  
300 data at high pressure allow us to observe a different behaviour among the three  
301 independent tetrahedra:  $T1$  and  $T2$  are essentially rigid (*i.e.*, difference in their bond  
302 lengths of the same order of the *e.s.ds*), but  $T3$  tends to deform significantly, in  
303 particular in response to the shortening of the  $T2-O2$  distance of about 0.03 Å (with  
304  $\Delta P = 8.5$  GPa; Table S2). Even among the three independent octahedra, we can  
305 observe different magnitude of (compression+distortion): within the  $P$ -range  
306 investigated, the maximum shortening of the intra-polyhedral bond lengths is  $\sim 0.04$  Å  
307 for the  $M2$  octahedron,  $\sim 0.06$  Å for the  $M1$  octahedron, and  $\sim 0.10$  Å for the  $M3$   
308 octahedron. Therefore, the Fe-rich  $M3$  octahedron is the most distorted one under  
309 hydrostatic compression, even in response to the pronounced  $T2-O8-M3$  compression  
310 described above.

311 One open question concerns the role played by the H-bonding scheme on the  $P$ -  
312 induced structure evolution of allanite. In allanite structure (as in all the epidote-group  
313 members), there is only one unique  $H$  site.  $O10$  acts as *donor* and  $O4$  acts as *acceptor*  
314 of the H-bond (*i.e.*,  $O10-H\dots O4$ );  $O4$  is the oxygen co-shared by two  $M1$  and one  $M3$   
315 octahedra and  $O10$  is the bridging oxygen between the edge-sharing  $M2$  octahedra.  
316 Proton, donor and acceptor are confined in the 5-membered ring. It is impossible to  
317 refine the  $H$  site coordinates in the HP structure refinements. However, we can  
318 intuitively consider that the H-bonding geometry can explain why in the 5-membered  
319 ring the major deformation mechanism acts on one side through the  $T1-O9-T2$  tilting,  
320 as the  $T1$  and  $T2$  tetrahedra are unaffected by the H-bonding. As a consequence, the  
321  $O3\leftrightarrow O1$  shortening is more pronounced than the  $O6\leftrightarrow O1$  and  $O9\leftrightarrow O5$  ones (Fig. 1,  
322 Tables S2 and 3).

323

## 324 Discussion and conclusions

325 To the best of our knowledge, this is the first study on the compressional  
326 behaviour of allanite, here described on the basis of *in-situ* synchrotron single-crystal  
327 diffraction data. The experimental findings of this study confirm that allanite  
328 preserves its crystallinity and behaves elastically at least up to 16 GPa (at 298 K),  
329 under hydrostatic compression (Table 2).

330 The Eulerian unit-strain ellipsoid, calculated between 0.0001 and 8.51 GPa,  
331 confirms that the lowest and the highest compression directions lie on the (010)-plane,  
332 as shown in Fig. 1: the softest direction ( $\epsilon_1$ ) describes an angle of  $136.6(2)^\circ$  from  
333 [100], and as a consequence the stiffest direction ( $\epsilon_3$ ) describes an angle of  $46.6(2)^\circ$   
334 from [100]. A recalculation of magnitude and orientation of the compressional unit-  
335 strain ellipsoids of epidote with 0.74 Fe a.p.f.u. (based on the data of Gatta et al.  
336 2011b, for  $\Delta P = 8.30$  GPa,  $P_{\min} = 0.0001$  GPa), of epidote with 0.79 Fe a.p.f.u. (based  
337 on the data of Qin et al. 2016, for  $\Delta P = 9.70$  GPa,  $P_{\min} = 0.0001$  GPa), and clinozoisite  
338 with 0.40 Fe a.p.f.u. (based on the data of Qin et al. 2016, for  $\Delta P = 8.80$  GPa,  $P_{\min} =$   
339  $0.0001$  GPa), was done, using the same Cartesian axial system and strain definition  
340 (*i.e.*, Eulerian) adopted for allanite:

- 341 1) in epidote with 0.79 Fe a.p.f.u., the stiffest direction ( $\epsilon_3 = -0.0232(2)$  GPa<sup>-1</sup>)  
342 is parallel to [010], whereas the mid ( $\epsilon_2 = -0.0236(3)$  GPa<sup>-1</sup>) and the softest  
343 ( $\epsilon_1 = -0.0258(8)$  GPa<sup>-1</sup>) directions lie on (010), with the softest one  
344 describing an angle of  $63(5)^\circ$  with [100]; anisotropic compressional scheme:  
345  $\epsilon_1:\epsilon_2:\epsilon_3 = 1.11:1.01:1$ , *i.e.* there is an almost circular section of the ellipsoid  
346 in which  $\epsilon_2$  and  $\epsilon_3$  are dispersed; the monoclinic  $\beta$  angle decreases  
347 monotonically with  $P$  (Qin et al. 2016);
- 348 2) in epidote with 0.74 Fe a.p.f.u., the stiffest direction ( $\epsilon_3 = -0.01646(8)$  GPa<sup>-1</sup>)  
349 is parallel to [010], whereas the mid ( $\epsilon_2 = -0.01978(8)$  GPa<sup>-1</sup>) and the  
350 softest ( $\epsilon_1 = -0.02352(6)$  GPa<sup>-1</sup>) directions lie on (010), with the softest one  
351 describing an angle of  $126.7(8)^\circ$  with [100]; anisotropic compressional  
352 scheme:  $\epsilon_1:\epsilon_2:\epsilon_3 = 1.43:1.20:1$ ; the monoclinic  $\beta$  angle decreases  
353 monotonically with  $P$  (Gatta et al. 2011b);
- 354 3) in clinozoisite (0.40 Fe a.p.f.u.), the stiffest direction ( $\epsilon_3 = -0.0138(2)$  GPa<sup>-1</sup>)  
355 is parallel to [010], whereas the mid ( $\epsilon_2 = -0.0145(2)$  GPa<sup>-1</sup>) and the  
356 softest ( $\epsilon_1 = -0.0234(1)$  GPa<sup>-1</sup>) directions lie on (010), with the softest one

357 describing an angle of  $174(1)^\circ$  with [100]; anisotropic compressional  
358 scheme:  $\epsilon_1:\epsilon_2:\epsilon_3 = 1.70:1.05:1$ ; the monoclinic  $\beta$  angle decreases  
359 monotonically with  $P$  (Qin et al. 2016).

360 On this basis, some general conclusions can be drawn:

- 361 1) The softest directions in allanite, epidote(s) and clinozoisite lie all on (010);
- 362 2) The stiffest directions in epidote and clinozoisite are consistently oriented  
363 parallel to [010], whereas in allanite it lies on (010) (*i.e.*,  $\epsilon_3 \angle [100] =$   
364  $46.6(2)^\circ$ );
- 365 3) The compressional schemes of allanite, epidote(s) and clinozoisite are  
366 significantly different: more anisotropic in allanite ( $\epsilon_1:\epsilon_2:\epsilon_3 = 2.18:1.47:1$ ),  
367 less in epidote ( $\epsilon_1:\epsilon_2:\epsilon_3 = 1.43:1.20:1$  with 0.74 Fe a.p.f.u, and  $\epsilon_1:\epsilon_2:\epsilon_3 =$   
368  $1.11:1.01:1$  with 0.79 Fe a.p.f.u) and clinozoisite ( $\epsilon_1:\epsilon_2:\epsilon_3 = 1.70:1.05:1$ ).
- 369 4) Concerning the joint epidote-clinozoisite, it is observable a drastic rotation of  
370 the unit-strain ellipsoid in response to the different Fe content: the softest  
371 direction describes an angle from [100] of  $174(1)^\circ$  in clinozoisite with 0.40 Fe  
372 a.p.f.u., of  $126.7(8)^\circ$  in epidote with 0.74 Fe a.p.f.u. and of  $63(5)^\circ$  in epidote  
373 with 0.79 Fe a.p.f.u., *i.e.* the lower the Fe content, the higher the angle  
374  $\epsilon_1 \angle [100]$ .

375 The stiffest direction can easily assume a different orientation in response to small  
376 compositional changes, due to the modest anisotropy observed ( $\epsilon_2:\epsilon_3 = 1.01:1$  and  
377  $1.20:1$  in epidote,  $1.05:1$  in clinozoisite, and  $1.47:1$  in allanite).

378 Our data on allanite show that the inter- and intra-polyhedral mechanisms,  
379 described on the basis of the structure refinements at high pressure, are not sufficient  
380 to explain, unambiguously, magnitude and orientation of the unit-strain ellipsoid. In  
381 this light, only some general considerations can be done:

- 382 1) The Eulerian unit-strain ellipsoid shows that the stiffest direction ( $\epsilon_3$ )  
383 lies on (010), it is perpendicular to the softest one and is likely governed  
384 by the presence of (almost incompressible) edge-sharing  $M3-M1-M3$   
385 clusters of octahedra (almost parallel to  $\epsilon_3$ ), connected to the  $A2$  sites  
386 (Fig. 1, Table S2).
- 387 2) The intermediate one ( $\epsilon_2$ ) is parallel to [010]. The compression of the  
388 allanite structure along [010] is likely hindered by the presence of the  
389 (infinite) edge-sharing  $M1O_6$  octahedral chains, running along [010]

390 (Fig. 1, Table S2). Edge-sharing octahedral chains act as “pillars”, and  
391 the shortening along the chain direction can only occur through intra-  
392 polyhedral deformation, by homogeneous or non-homogeneous (*i.e.*,  
393 polyhedral distortion) bond-distances compression.

394 3) The most compressible direction ( $\epsilon_1$ , as defined above) in allanite  
395 structure lies also on (010). Tilting and (compression+distortion) of the  
396 polyhedra, described above, generate, in turns, the deformations of the  
397 5- and 8-membered rings of polyhedra. The most pronounced  
398 compression directions of the rings (represented *e.g.* by the diameters  
399  $O3 \leftrightarrow O1$  of the 5-membered ring and by  $O8 \leftrightarrow O8$  of the 8-membered  
400 ring) can play an important role on the orientation of  $\epsilon_1$  (Fig. 1, Table  
401 S2).

402 The compressional elastic anisotropy described on the basis of the “linearised  
403 bulk moduli” along the three crystallographic axes, all obtained on the basis of a  
404 second-order BM-EoS fit (as the truncation to second-order provide the best figures of  
405 merit), is:  $K_{P0,T0}(a):K_{P0,T0}(b):K_{P0,T0}(c) = 1.24:1.52:1$  in allanite,  $K_{T0}(a):K_{T0}(b):K_{T0}(c) =$   
406  $1.13:1.48:1$  in epidote with 0.74 Fe a.p.f.u. (recalculated from Gatta et al. 2011b) and  
407  $K_{T0}(a):K_{T0}(b):K_{T0}(c) = 1:1.19:1.04$  in epidote with 0.79 Fe a.p.f.u. (Qin et al. 2016),  
408 and  $K_{P0,T0}(a):K_{P0,T0}(b):K_{P0,T0}(c) = 1:1.81:1.52$  in clinozoisite with 0.40 Fe a.p.f.u.  
409 (Qin et al. 2016).

410 The bulk compression of allanite, epidote and clinozoisite is significantly  
411 different (Fig. 2). Using a third-order BM-EoS, the following parameters are obtained:  
412  $K_{P0,T0}=131(4)$  GPa and  $K'=1.9(8)$  for allanite,  $K_{P0,T0}=111(3)$  GPa and  $K'=7.6(7)$  for  
413 epidote with 0.74 Fe a.p.f.u. (Gatta et al. 2011b) and  $K_{P0,T0}=115(2)$  GPa and  
414  $K'=3.7(2)$  for epidote with 0.79 Fe a.p.f.u. (Qin et al. 2016), and  $K_{P0,T0}=142(3)$  GPa  
415 and  $K'=5.2(4)$  for clinozoisite with 0.40 Fe a.p.f.u. (Qin et al. 2016). Epidote is the  
416 softest one, clinozoisite is the stiffest and allanite lies in between.

417 On the basis of a comparative analysis of the compressional behavior of  
418 epidotes and clinozoisites reported in the literature, along with those obtained  
419 experimentally in their study, Qin et al. (2016) concluded that increasing Fe content  
420 reduces the bulk modulus and increases the first *P*-derivative (using the BM-EoS  
421 formulation). This behavior was attributed to the differences in compression behavior  
422 due to the addition of Fe at the *M3* site (replacing Al) in the epidote structure.

423 Additional *in-situ* HP Raman data collected by Qin et al. (2016) further suggest that  
424 the difference in compressibility between epidote and clinozoisite is likely to be  
425 different compressibility of FeO<sub>6</sub>- and AlO<sub>6</sub>-octahedra, coordinated by the M3 sites.  
426 In allanite, the scenario is more complex: Fe and Al mainly populate the octahedral  
427 sites (Fe occurs principally at the M3 site, like in epidote), but a fraction of Al likely  
428 replaces Si at the tetrahedral sites and, more important, Fe along with a series of other  
429 LREE elements (mainly Ce and La) replace Ca at the A1 and A2 sites. In this light, the  
430 conclusion of Qin et al (2016), about the role played by iron content on the  
431 compressional behavior, cannot be simplistically extended to allanite, as more  
432 variables can influence the different behavior of allanite if compared to the other two  
433 aforementioned members of the epidote group.

434

### 435 **Acknowledgements**

436 PETRA-III synchrotron facility (Hamburg, Germany) is acknowledged for provision  
437 of beamtime at P02.2 beamline. G.D.G., S.M., L.C., D.C., P.L., M.M. acknowledge  
438 the support of the Italian Ministry of Education (MIUR) through the project  
439 “Dipartimenti di Eccellenza 2018–2022”. W. Crichton and an anonymous reviewer  
440 are thanked for the revision of the manuscript.

441

442

### 443 **References**

444 Angel RJ (2000) Equation of State. In: Hazen RM, Downs RT (eds) High-  
445 temperature and high-pressure crystal chemistry. Reviews in Mineralogy and  
446 Geochemistry, vol. 41, Mineralogical Society of America and Geochemical Society,  
447 Washington, DC, pp 35-59.

448 Angel RJ, Bujak M, Zhao J, Gatta GD, Jacobsen SD (2007) Effective  
449 hydrostatic limits of pressure media for high-pressure crystallographic studies. J Appl  
450 Crystallogr 40:26–32.

451 Armbruster T, Bonazzi P, Akasaka M, Bermanec V, Chopin C, Gieré R, Heuss-  
452 Assbichler S, Liebscher A, Menchetti S, Pan Y, Pasero M (2006) Recommended  
453 nomenclature of epidote-group minerals. Eur J Mineral 18:551-567.

454 Birch F (1947) Finite elastic strain of cubic crystal. Phys Rev 71:809-824.

455 Bird DK, Helgeson HC (1980) Chemical interaction of aqueous solutions with

456 epidote-feldspar mineral assemblages in geologic systems, I: thermodynamic analysis  
457 of phase relations in the system CaO-FeO-Fe<sub>2</sub>O<sub>3</sub>-Al<sub>2</sub>O<sub>3</sub>-SiO<sub>2</sub>-H<sub>2</sub>O-CO<sub>2</sub>. Am J Science  
458 280:907–941.

459 Bird DK, Cho M, Janik CJ, Liou JG, Caruso LJ (1988) Compositional, order-  
460 disorder, and stable isotopic characteristics of Al-Fe epidote, state 2–14 drill hole,  
461 Salton Sea geothermal system. J Geophys Res 93(B11):13135-13144.

462 Bonazzi P, Holtstam D., Bindi L., P. Nysten, Capitani G.C. (2009) Multi-  
463 analytical approach to solve the puzzle of an allanite-subgroup mineral from Kesebol,  
464 Västra Götaland, Sweden. Am Mineral 94: 121-134.

465 Catti M, Ferraris G, Ivaldi G (1988) Thermal behaviour of the crystal structure  
466 of strontian piemontite. Am Mineral 73:1370-1376.

467 Comodi P, Zanazzi PF (1997) The pressure behaviour of clinozoisite and  
468 zoisite. An X-ray diffraction study. Am Mineral 82:61-68.

469 Corti L, Alberelli G, Zanoni D, Zucali M (2017) Analysis of fabric evolution  
470 and metamorphic reaction progress at Lago della Vecchia-Valle d'Irona, Sesia-  
471 Lanzo Zone, Western Alps. J Maps 13:521-533.

472 Corti L, Alberelli G, Zanoni D, Zucali M (2018) Tectonometamorphic evolution  
473 of the Lago della Vecchia metaintrusive and its country rocks, Sesia-Lanzo Zone,  
474 Western Alps. Ital J Geosci 137:188-207.

475 Corti L, Zanoni D, Gatta GD, Zucali M (2019) Shielding effect in allanite as to-  
476 mantle carrier of LREE: strain, chemistry, and crystallographic constraints. Geology  
477 (*under revision*).

478 Dollase WA (1971) Refinement of the crystal structure of epidote, allanite and  
479 hancockite. Am Mineral 56:447-464.

480 Franz G, Liebscher A (2004) Physical and chemical properties of epidote  
481 minerals – An Introduction. In Franz G, Liebscher A (eds), Epidotes, Vol. 56, p. 1-81.  
482 Reviews in Mineralogy and Geochemistry, Mineralogical Society of America and  
483 Geochemical Society, Washington, U.S.A.

484 Gatta GD, Meven M, Bromiley G (2010) Effects of temperature on the crystal  
485 structure of epidote: a neutron single-crystal diffraction study at 293 and 1,070 K.  
486 Phys. Chem. Minerals 37:475-485.

487 Gatta G.D., Alvaro M., Bromiley G. (2011a) A low temperature X-ray single-

488 crystal diffraction and polarised infra-red study of epidote. *Phys. Chem. Minerals*  
489 39:1–15.

490 Gatta G.D., Merlini M., Lee Y., Poli S. (2011b) Behavior of epidote at high  
491 pressure and high temperature: a powder diffraction study up to 10 GPa and 1,200 K.  
492 *Phys. Chem. Minerals* 38:419-428.

493 Gieré R, Sorensen SS (2004) Allanite and other REE-rich epidote-group  
494 minerals. In: Franz G, Liebscher A (eds), *Epidotes*, Vol. 56, p. 431-493. *Reviews in*  
495 *Mineralogy and Geochemistry*, Mineralogical Society of America and Geochemical  
496 Society, Washington, U.S.A..

497 Heinz DL, Jeanloz R (1984) The equation of state of the gold calibration  
498 standard. *J Appl Phys* 55:885-893.

499 Holdaway MJ (1972) Thermal stability of Al-Fe epidotes as a function of  $fO_2$   
500 and Fe content. *Contrib Min Petrol* 37:307–340.

501 Holland TJB, Redfern SAT, Pawley AR (1996) Volume behaviour of hydrous  
502 minerals at high pressure and temperature: II. Compressibilities of lawsonite, zoisite,  
503 clinozoisite, and epidote. *Am Mineral* 81:341-348.

504 Klemm R (2004) Fluid inclusions in epidote minerals and fluid development in  
505 epidote-bearing rocks. In: Franz G, Liebscher A (eds), *Epidotes*, Vol. 56, p. 197-234.  
506 *Reviews in Mineralogy and Geochemistry*, Mineralogical Society of America and  
507 Geochemical Society, Washington, U.S.A..

508 Klotz S, Chervin J-C, Munsch P, Le Marchand G (2009) Hydrostatic limits of  
509 11 pressure transmitting media. *J Phys D: Appl Phys* 42: 075413 (7pp).

510 Liebscher A (2004) Spectroscopy of epidote minerals. In: Franz G, Liebscher A  
511 (eds), *Epidotes*, Vol. 56, p. 125-170. *Reviews in Mineralogy and Geochemistry*,  
512 Mineralogical Society of America and Geochemical Society, Washington, U.S.A..

513 Liou JG (1973) Synthesis and stability relations of epidote,  
514  $Ca_2Al_2FeSi_3O_{12}(OH)$ . *J Petrol* 14:381–413.

515 Mao HK, Xu J, Bell PM (1986) Calibration of the ruby pressure gauge to 800 kbar  
516 under quasi-hydrostatic conditions. *J Geophys Res* 91:4673-4676.

517 Pawley AR, Redfern SAT, Holland TJB (1996) Volume behaviour of hydrous  
518 minerals at high pressure and temperature: 1. Thermal expansion of lawsonite, zoisite,  
519 clinozoisite, and diaspore. *Am Mineral* 81:335-340.

520 Poli S, Schmidt MW (1998) The high-pressure stability of zoisite and phase  
521 relationships of zoisite-bearing assemblages. *Contrib Mineral Petrol* 130:162-175.

522           Qin F, Wu X, Wang Y, Fan D, Qin S, Yang K, Townsend JP, Jacobsen SD  
523 (2016) High-pressure behavior of natural single-crystal epidote and clinozoisite up to  
524 40 GPa. *Phys Chem Minerals* 43:649-659.

525           Rothkirch A, Gatta GD, Meyer M, Merkel S, Merlini M, Liermann H-P (2013)  
526 Single-crystal diffraction at the Extreme conditions beamline P02.2: procedure for  
527 collecting and analyzing high-pressure single-crystal data. *J Synchrotron Rad* 20:711–  
528 720.

529           Schmidt MW, Poli S (2004) Magmatic epidotes. In G. Franz and A. Liebscher,  
530 Eds., *Epidotes*, Vol. 56, p. 399-430. *Reviews in Mineralogy and Geochemistry*,  
531 Mineralogical Society of America and Geochemical Society, Washington, U.S.A.

532           Sheldrick GM (1997) SHELX-97. Programs for crystal structure determination  
533 and refinement. University of Göttingen, Germany.

534           Sheldrick GM (2008) A short history of SHELX. *Acta Cryst A* 64:112-122.

535  
536

537  
538  
539  
540  
541  
542

Table 1. Lattice parameters of allanite at different pressures, based on the two datasets collected using the methanol:ethanol:water mix (HP-mew) and neon (HP-Ne) as  $P$ -transmitting fluids ( $P$ -uncertainty:  $\pm 0.1$  GPa)

Experiment	$P$ (GPa)	$a$ (Å)	$b$ (Å)	$c$ (Å)	$\beta$ (Å)	$V$ (Å <sup>3</sup> )
HP-mew <sup>a</sup>	0.0001	8.9116(3)	5.738(2)	10.1447(4)	114.979(4)	470.2(2)
HP-mew <sup>b</sup>	0.0001	8.9130(2)	5.735(2)	10.1484(3)	114.993(3)	470.2(2)
HP-mew	1.17	8.8882(4)	5.719(2)	10.1071(4)	114.872(6)	466.1(2)
HP-mew	1.60	8.8781(4)	5.712(2)	10.0911(3)	114.832(5)	464.42(9)
HP-mew	1.97	8.8718(4)	5.707(2)	10.0821(4)	114.805(5)	463.4(1)
HP-mew	2.81	8.8497(2)	5.697(8)	10.0509(2)	114.707(3)	460.33(7)
HP-mew	3.30	8.8416(4)	5.6890(2)	10.0383(4)	114.684(5)	458.8(1)
HP-mew	3.61	8.8325(3)	5.6880(9)	10.0293(3)	114.647(3)	457.96(7)
HP-mew	3.99	8.8223(2)	5.6834(8)	10.0152(2)	114.593(3)	456.62(7)
HP-mew	4.86	8.7996(3)	5.674(1)	9.9865(3)	114.519(4)	453.63(8)
HP-mew	5.08	8.7963(2)	5.6686(9)	9.9813(2)	114.512(3)	452.84(7)
HP-mew	5.55	8.7851(2)	5.6657(9)	9.9667(2)	114.462(3)	451.55(7)
HP-mew	6.45	8.7655(2)	5.6550(9)	9.9412(2)	114.388(3)	448.80(7)
HP-mew	7.07	8.7466(3)	5.644(2)	9.9177(3)	114.321(4)	446.2(1)
HP-mew	7.61	8.7384(3)	5.638(2)	9.9073(3)	114.287(4)	444.94(9)
HP-mew	8.51	8.7231(3)	5.629(2)	9.8817(3)	114.225(4)	442.50(9)
HP-Ne <sup>c</sup>	1.39	8.8881(6)	5.7303(3)	10.111(2)	114.88(2)	467.2(2)
HP-Ne <sup>c</sup>	9.90	8.668(3)	5.6171(2)	9.839(6)	113.87(6)	438.1(3)
HP-Ne <sup>c</sup>	14.64	8.563(3)	5.5643(2)	9.722(7)	113.56(7)	424.6(4)

<sup>a</sup>Sample in the DAC without  $P$ -medium

<sup>b</sup>After decompression.

<sup>c</sup>For the experiments in Ne, the  $P$ -value at any data point represents the average value obtained by the ruby-fluorescence method and the BM-EoS fit based on the *mew* experiments.



Table 3. Principal “diameters” (Å) of the 8-membered ring (O6↔O10, O3↔O3, O6↔O6 and O8↔O8) and of the 5-membered one (O3↔O1, O6↔O1, O9↔O5) at different pressures (*P*-uncertainty: ±0.1 GPa).

Experiment	<i>P</i> (GPa)	O6↔O10	O3↔O3	O6↔O6	O8↔O8	O3↔O1	O6↔O1	O9↔O5
HP-mew <sup>a</sup>	0.0001	7.032(9)	7.297(10)	7.702(9)	4.778(8)	3.615(5)	4.364(11)	4.674(5)
HP-mew	1.17	7.011(10)	7.251(14)	7.677(7)	4.707(8)	3.606(5)	4.352(15)	4.672(5)
HP-mew	1.60	7.005(9)	7.251(12)	7.668(7)	4.691(9)	3.601(5)	4.349(13)	4.669(5)
HP-mew	1.97	7.001(12)	7.245(10)	7.660(9)	4.682(11)	3.596(6)	4.347(13)	4.672(6)
HP-mew	3.61	6.971(8)	7.198(8)	7.637(9)	4.624(10)	3.581(5)	4.338(9)	4.671(6)
HP-mew	3.99	6.968(7)	7.184(8)	7.631(7)	4.619(9)	3.579(5)	4.337(9)	4.655(5)
HP-mew	4.86	6.951(9)	7.162(10)	7.612(9)	4.587(9)	3.571(5)	4.332(11)	4.652(5)
HP-mew	5.08	6.948(8)	7.159(8)	7.612(9)	4.581(10)	3.568(5)	4.334(9)	4.657(6)
HP-mew	5.55	6.942(8)	7.146(8)	7.610(9)	4.560(10)	3.563(5)	4.326(9)	4.651(6)
HP-mew	6.45	6.925(8)	7.131(8)	7.592(9)	4.538(9)	3.554(5)	4.321(9)	4.649(6)
HP-mew	7.07	6.912(10)	7.119(11)	7.579(10)	4.515(11)	3.543(6)	4.314(12)	4.644(7)
HP-mew	7.61	6.901(8)	7.114(10)	7.566(9)	4.502(9)	3.539(4)	4.314(11)	4.644(5)
HP-mew	8.51	6.883(8)	7.101(10)	7.547(7)	4.478(9)	3.531(4)	4.309(11)	4.643(5)

<sup>a</sup>Sample in the DAC without *P*-medium

Table 4. Compressional parameters of allanite obtained by second- and third-order Birch-Murnaghan Equation of State fits (see text for details).

	$V_0, l_0$ ( $\text{\AA}^3, \text{\AA}$ )	$K_{P_0, T_0}$ (GPa)	$K'$	$EoS$ order
$V_0$	470.6(2)	122(1)	4 (fixed)	2 <sup>nd</sup> order
$a_0$	8.918(3)	114(2)	4 (fixed)	2 <sup>nd</sup> order
$b_0$	5.735(2)	140(4)	4 (fixed)	2 <sup>nd</sup> order
$c_0$	10.149(2)	92(1)	4 (fixed)	2 <sup>nd</sup> order
$V_0$	470.2(2)	131(4)	1.9(8)	3 <sup>rd</sup> order

Figure 1. Crystal structure of allanite viewed down [010] and [001], and overlying unit-strain ellipsoid based on Eulerian finite strain calculated between ambient pressure and 8.51 GPa [ $\epsilon_2 // b$ ,  $\epsilon_1$  and  $\epsilon_3$  lying in the (010)-plane,  $\epsilon_1 \angle a = 136.6(2)^\circ$ ;  $\epsilon_1 = -0.02849(5)$ ,  $\epsilon_2 = -0.0192(5)$ , and  $\epsilon_3 = -0.01306(8)$  GPa<sup>-1</sup>,  $\epsilon_1 : \epsilon_2 : \epsilon_3 = 2.18 : 1.47 : 1$ ]. Si-tetrahedra (coordinated by  $Si1$ ,  $Si2$  and  $Si3$  sites) and Al/Fe-octahedra (coordinated by the  $M1$ ,  $M2$  and  $M3$  sites) are shown as closed-faces polyhedra; large spheres represent the  $A1$  and  $A2$ -sites. The 8-membered ring of polyhedra (with the diameters  $O3 \leftrightarrow O3$ ,  $O10 \leftrightarrow O6$ ,  $O6 \leftrightarrow O6$  and  $O8 \leftrightarrow O8$ ) and the 5-membered ring (with the diameters  $O3 \leftrightarrow O1$ ,  $O1 \leftrightarrow O6$  and  $O9 \leftrightarrow O5$ ) are also shown (see text for further details).

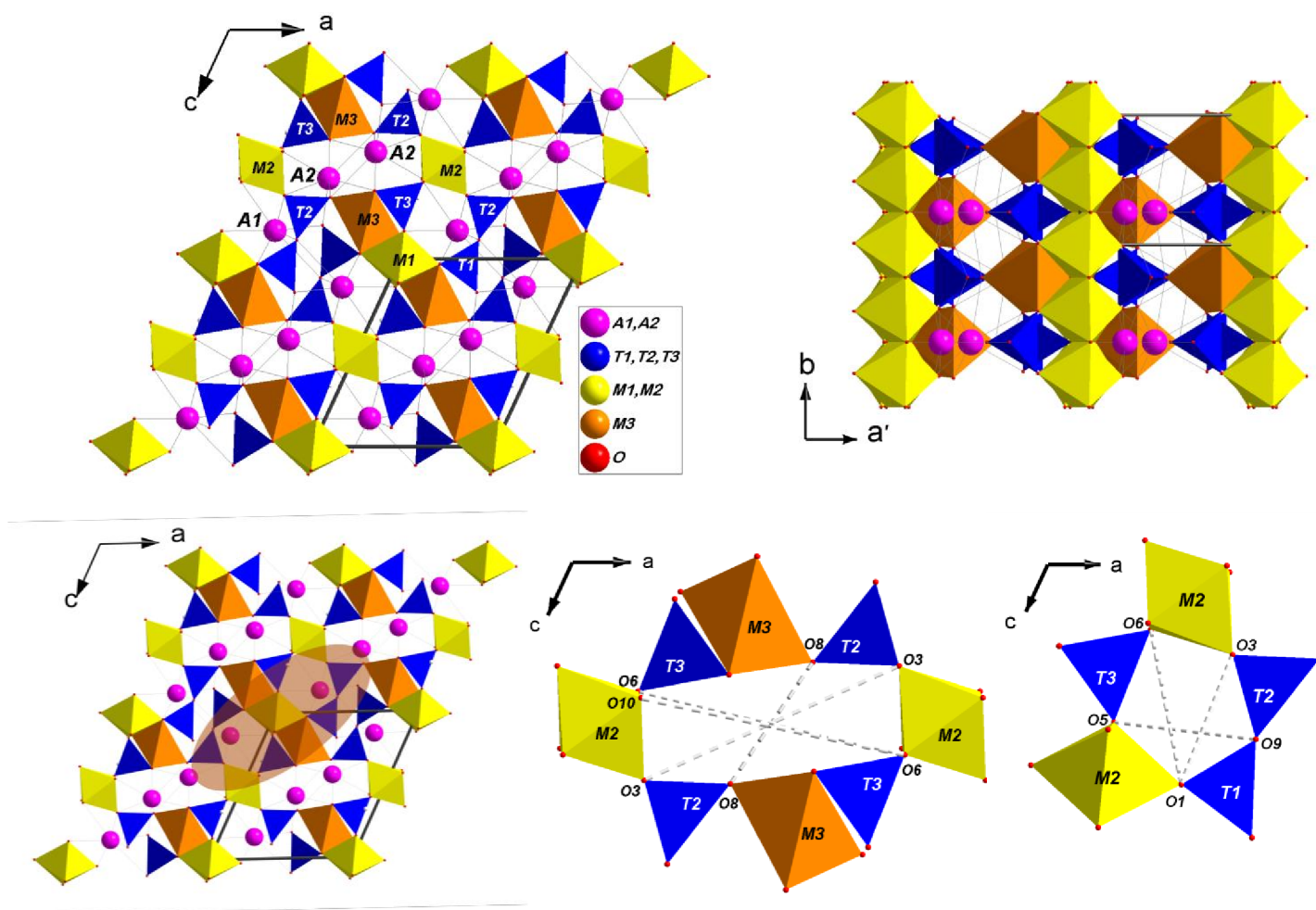
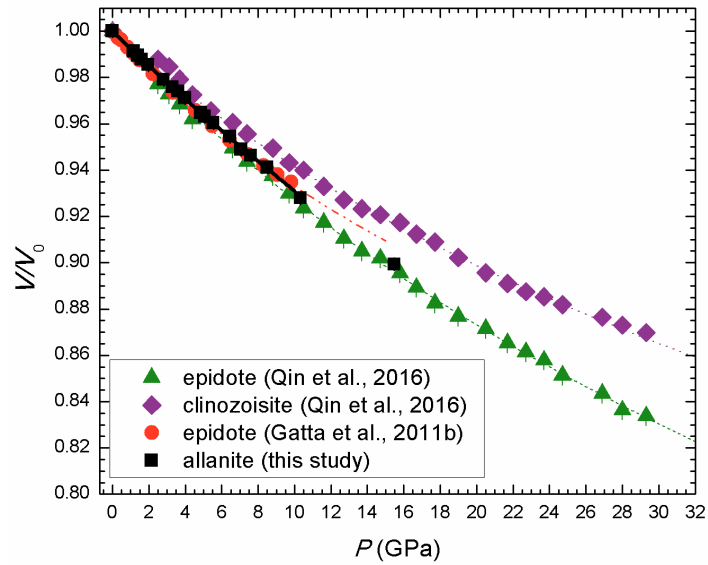
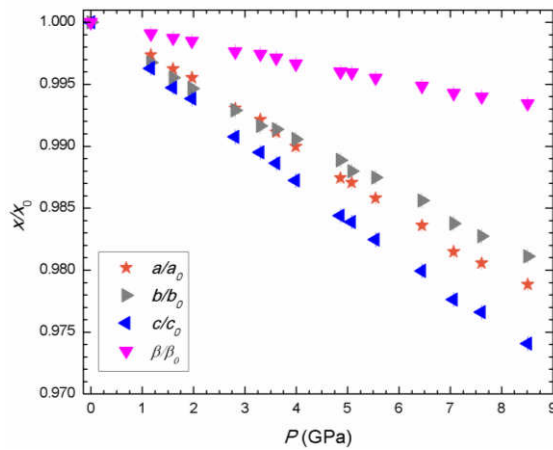


Figure 2. Evolution of the lattice parameters of allanite with  $P$  (GPa). (a) For the unit-cell volume, the solid lines represent the third-order BM-EoS fits. The axial compressional behaviours of (b) allanite (this study), (c) epidotes with 0.74 Fe a.p.f.u. (Gatta et al. 2011b), (d) epidotes with 0.79 Fe a.p.f.u. (Qin et al. 2016), and (e) clinozoisite with 0.40 Fe a.p.f.u. (Qin et al. 2016) are also shown.

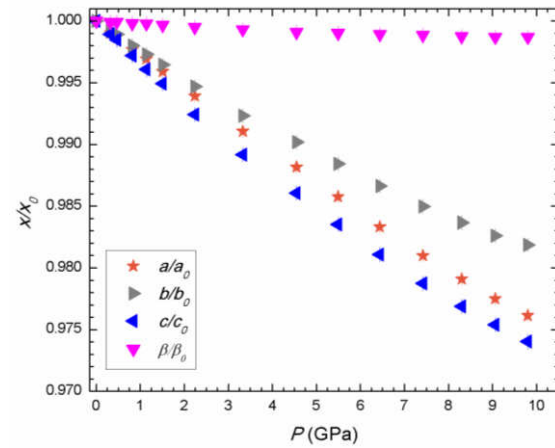
a)



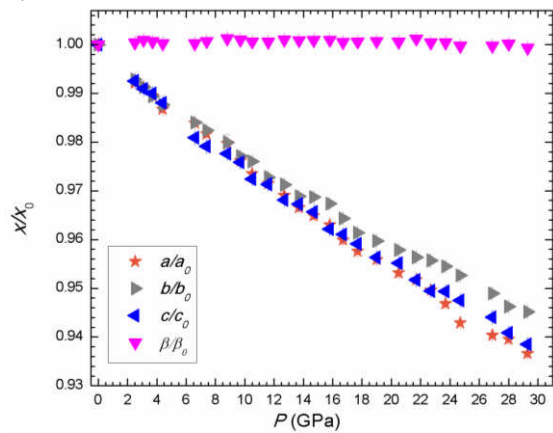
b)



c)



d)



e)

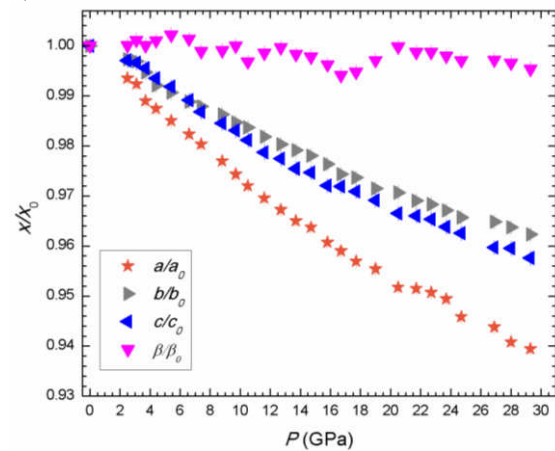


Figure 3. Normalized stress ( $F_e = P/[3fe(1+2fe)^{5/2}]$ ) vs. Eulerian finite strain ( $fe = [(V_0/V)^{2/3} - 1]/2$ ) plot. The *esds* have been calculated according to Heinz and Jeanloz (1984). The solid line is a weighted linear fit through the data.

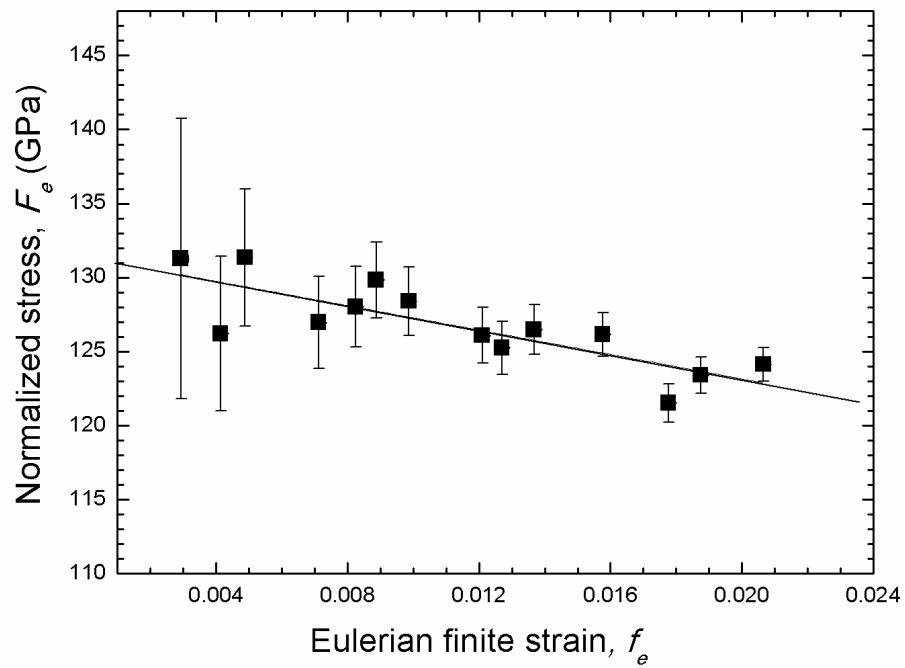


Figure 4. Confidence ellipses at 68.3% level ( $\Delta\chi^2=2.30, \pm 1\sigma$ , solid black line), 95.4% level ( $\Delta\chi^2=6.17, \pm 2\sigma$ , dashed black line) and 99.7% level ( $\Delta\chi^2=11.8, \pm 3\sigma$ , dotted black line) calculated starting from the variance-covariance matrix of  $K_{P_0,T_0}$  and  $K'$  obtained from the least-square procedure. The  $K_{P_0,T_0}$  and  $K'$  of Gatta et al. (2011b) for epidote (0.74 Fe a.p.f.u.; red circle), of Qin et al. (2016) for epidote (0.79 Fe a.p.f.u.; dark green triangle), and of Qin et al. (2016) for clinozoisite (0.40 Fe a.p.f.u.; purple diamond) are added for comparison (see text for further details). Error bars:  $\pm 1$  esds.

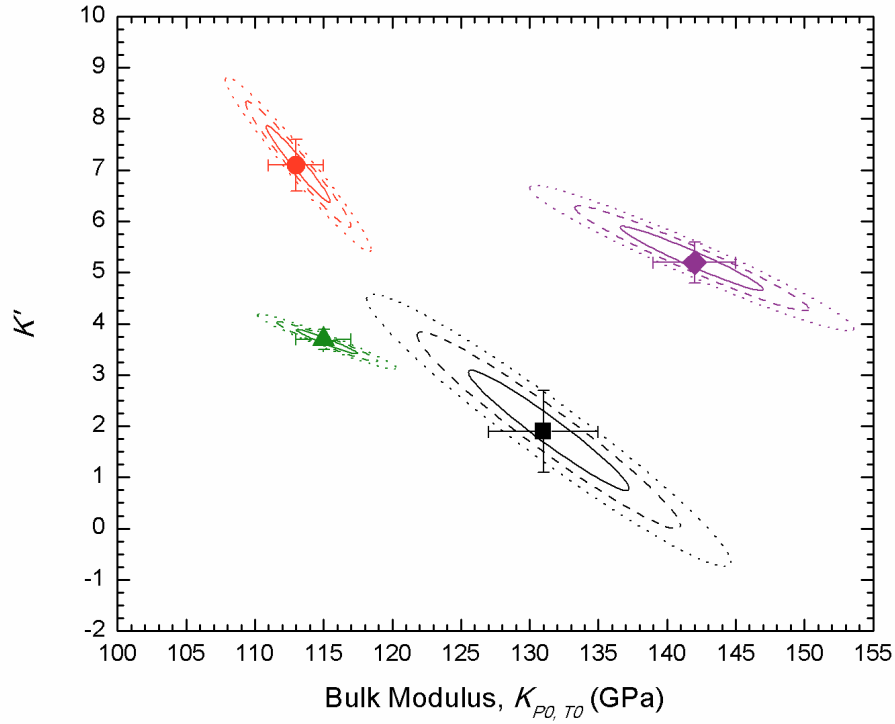


Figure 5. Evolution with  $P$  of the (normalised)  $O3\leftrightarrow O3$ ,  $O6\leftrightarrow O6$ ,  $O8\leftrightarrow O8$  and  $O10\leftrightarrow O6$  “diameters” of the 8-membered ring of polyhedra, and of the  $O3\leftrightarrow O1$ ,  $O1\leftrightarrow O6$  and  $O9\leftrightarrow O5$  “diameters” of the 5-membered ring (see Fig. 1 and text for further details).

